Journal of The Electrochemical Society, **161** (1) A109-A117 (2014)
0013-4651/2014/161(1)/A109/9/$31.00 © The Electrochemical Society

A Computationally-Effective Thermal Model for Spirally Wound Nickel-Metal Hydride Batteries

Maryam Yazdanpour,[*] Peyman Taheri,[**] and Majid Bahrami[z]

Laboratory for Alternative Energy Conversion (LAEC), School of Mechatronic Systems Engineering, Simon Fraser University, Surrey, BC V3T 0A3, Canada

A new two-dimensional analytical model is developed to investigate the transient thermal behavior of spirally wound batteries. The proposed model is used to analyze the thermal response of a 8 ampere-hour cylindrical nickel-metal hydride (NiMH) battery under fast-charging processes with overcharging periods. Based on the method of integral transformation, a series-form solution for the temperature field in cylindrical batteries is obtained that takes account for transient heat generation, orthotropic heat conduction, and convective heat dissipation. The accuracy of the theoretical solution is tested through comparison with numerical solution and experimental data. Our comparisons show that even the first term of the series solution suffices to accurately describe the two-dimensional temperature field inside the battery core with the modest computational effort.
 [DOI: 10.1149/2.047401jes]

Manuscript submitted September 13, 2013; revised manuscript received October 29, 2013. Published November 16, 2013.

Many battery systems produce heat while in operation due to the exothermic nature of the electrochemical processes involved. This buildup heat, if not managed properly, results in significant temperature rise inside the battery, which may strongly affect its performance, longevity, and in extreme cases leads to serious safety hazards such as fire and explosion. Moreover, exposure of batteries to sub-freezing temperatures drastically reduces their energy and power delivery. Accordingly, reliable battery thermal models are highly on demand to predict the heat generation and its transport inside batteries, and design efficient thermal management systems depending upon the cell design and operation conditions.

Detailed thermal models for batteries require extensive numerical effort owing to their multi-layered structure and simultaneous occurrence of thermal, electrical, and chemical processes. Thanks to the fast-paced development of computational tools, such simulations that involve complex steps such as geometry modeling, mesh generation, intense computations, and post-processing have become accessible for chemistry optimization and electrode design. Nonetheless, detailed battery simulations are still affordable only at electrode level, and for scale-up batteries (stack of electrodes) such simulations are not plausible computationally; instead, standalone thermal models or electro-thermal models with focus on thermal response of the battery under different operating conditions are favorable.

To the authors' best knowledge, multi-dimensional thermal models for cylindrical batteries are all based on numerical approaches[1-10] and lack of analytical solution is apparent in the literature. From the computational point of view, analytical solutions are highly on demand because they are continuous in the independent variables, and show explicitly how the parameters of the system are involved. Furthermore, analytical solutions give much insight into a system, which is one of the primary objectives of modeling. To date, only zero-dimensional (lumped) and one-dimensional (radial direction) thermal models for cylindrical batteries are available, for example see Ref. 11. Accordingly, in the present study, a two-dimensional analytical thermal model is developed for cylindrical batteries. This paper forms a sequel to our previous works[12,13] where a computationally-effective three-dimensional thermal model was developed to describe the transient thermal behavior of prismatic batteries; here, we have adapted the methodology to cylindrical geometry. Indeed, this is a challenging task due to complexity of the governing equations at the presence of spatial curvature.

In our approach, we use the method of integral transform to obtain a series-form solution for the energy equation with orthotropic thermal conductivities, unsteady heat generation, and convective boundary conditions. It is important to emphasize that the proposed model is general and can be used to investigate the fundamental problem of heat conduction in all spirally wound batteries with different chemistries. However, for the sake of demonstration, we have applied the model to a 8 Ah spirally wound nickel-metal hydride (NiMH) battery under fast-charging processes (with constant currents) in order to highlight its capabilities.

The analytical solutions for the sample NiMH cell are compared to those of accurate numerical simulations and experimental data available in the literature.[1] The comparisons show favorable agreement with both numerical and experimental data. More importantly, it is shown that the analytical series-form solution rapidly converges to the numerical solution and fairly matches with the experimental measurements. Indeed, its leading terms provide a simple yet accurate approximation of the battery thermal behavior with modest numerical effort.

In the following sections, details of the theoretical thermal model are explained and its implementation to the sample NiMH cell is demonstrated. Evolution of the temperature field inside the battery core is discussed for different charging rates, while natural- and forced-convective cooling conditions are assumed.

Thermal Model

Model Assumptions.— The main challenges in thermal modeling of large-scale batteries are;

i) evaluation of the heat generation rate,
ii) incorporating the effects of convective heat transfer inside the battery,
iii) dependency of thermophysical parameters on temperature,
iv) treatment of heat conduction in multi-layer structure of the battery core.

To evaluate the battery heat generation, a common practice is to use direct or indirect calorimetry techniques.[6,14] An alternative approach is to approximate the heat generation rate from electrical performance of the battery, i.e., experimental voltage-time data.[1,15] In the present paper the latter approach is employed to approximate the heat generation rate in the sample NiMH cell during rapid-charging processes with overcharging periods.

Also, due to the porosity of battery components, the motion of the electrolyte is neglected, thus the convective terms do not appear in our analysis.

Furthermore, to find an analytical solution, we assume that thermophysical properties are not temperature dependent, which is a valid assumption for batteries with a narrow range for temperature change during their operation.

Often, standalone thermal modeling for large-scale batteries is accomplished by assuming that the different components of the battery interior can be represented by a homogeneous region (i.e., core region)

[*]Electrochemical Society Student Member.
[**]Electrochemical Society Active Member.
[z]E-mail: mbahrami@sfu.ca

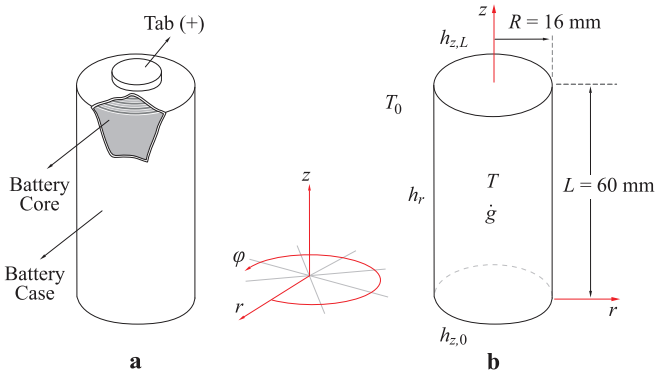

Figure 1. (a) Multi-layered structure of a cylindrical NiMH battery, (b) Two-dimensional schematic of the battery core in *r*-*z* plane with internal heat generation $\dot{g}$, and convective heat dissipation at boundaries.

have average properties. This approach, which is used in our analysis, greatly simplifies the analysis and is essential to obtain an analytical solution for the problem; however, it may not provide adequate results when the different components of the battery have very different thermal properties.[16]

Model Formulation.— A 8 Ah cylindrical NiMH battery is considered in this study to demonstrate the modeling steps and validate the results. For the considered battery, experimental data during rapid-charging processes with overcharging periods are reported in Ref. 1.

As illustrated in Fig. 1a, the radius and height of the battery are 16.5 mm and 60.5 mm, respectively. In our analysis we divide the battery into two regions: the core region, and the case region (can).The battery core ($R \times L = 16 \times 60$ mm), shown in Fig. 1b, includes a positive nickel electrodes, a negative metal hydride electrodes, and a polypropylene separator sheet. All components of the core are porous and their pores are filled with a concentrated KOH solution (30 wt%) which acts as the electrolyte. At positive and negative electrodes $\beta-Ni(OH)_2$ and Mm $Ni_{3.75}$ $Co_{0.55}$ $Al_{0.3}$ $Mn_{0.4}$ are used as active materials, respectively. All components of the battery core are spirally wound and packaged in a stainless steel container, i.e., the case region, with the thickness of 0.5 mm.

Values of volume fraction, porosity, and thermal conductivity for the battery components are listed in Table I, borrowed from Ref. 1.

The values of thermal conductivity for dry electrodes and dry separator are given in Table I. To evaluate thermal conductivities of wet electrodes and separator, it is assumed that their pores are fully filled with the electrolyte liquid, and their thermal conductivities are approximated as,[17]

$$k = k_m(1-\varepsilon) + k_f\,\varepsilon \qquad [1]$$

where ε is the porosity, listed in Table I. The subscripts 'm' and 'f' correspond to structural materials (electrodes and separator), and liquid filler (electrolyte), respectively.

As stated in Section Model Assumptions, in order to avoid complexities associated with heat transfer in multi-layered structure of the battery core, we use the concept of equivalent thermal resistance network to define effective thermal conductivities for the battery core. Based on Fig. 1a, there are series thermal resistors in *r*-direction and parallel thermal resistors in *z*-directions. Therefore, by using the data from Table I, through-plane (*r*-direction) and in-plane (*z*-direction) thermal conductivities can be evaluated as,[1]

Table I. Volume fraction, porosity, and thermal conductivity of battery components.[1]

Material/Layer	Volume fraction of battery core ν [%]	Porosity ε	Thermal conductivity k [W m^{-1} K^{-1}]
Porous negative electrode	28	0.25	1.16
Porous positive electrode	45	0.30	1.14
Porous separator sheet	27	0.74	0.22
Electrolyte	–	–	0.57
Case	–	–	16

$$k_r = \left(\sum_i \frac{\nu_i}{k_i}\right)^{-1} = \left(\frac{\nu_p}{k_p} + \frac{\nu_s}{k_s} + \frac{\nu_n}{k_n}\right)^{-1} = 0.74\,[\mathrm{W\,m^{-1}\,K^{-1}}] \qquad [2a]$$

and

$$k_z = \sum_i \nu_i k_i = \nu_p k_p + \nu_s k_s + \nu_n k_n = 0.85\,[\mathrm{W\,m^{-1}\,K^{-1}}] \qquad [2b]$$

where ν_p, ν_s, and ν_n represent the volume fraction of the positive electrode, separator, and negative electrode, respectively. The thermal conductivity of positive electrode k_p, negative electrode k_n, and separator k_s at the presence of electrolyte liquid are obtained from Eq. (1).

By assuming that temperature has no variation in azimuthal direction (φ-direction), the transient temperature field inside the battery core can be described by the energy balance equation in cylindrical coordinates,[1,2,8]

$$\rho c_p \frac{\partial T}{\partial t} = k_z \frac{\partial^2 T}{\partial z^2} + k_r \frac{1}{r}\frac{\partial}{\partial r}\left(r\frac{\partial T}{\partial r}\right) + \dot{g} \qquad [3]$$

in which t is the time, while r and z represent the components of the position vector in cylindrical coordinate system. The functions $T(r, z, t)$ and $\dot{g}(r, z, t)$ denote the temperature field and volumetric heat generation rate inside the battery core, respectively (Fig. 1b). The density ρ, specific heat c_p, and orthotropic thermal conductivities k_r and k_z [cf. Eq. (2)] are the thermophysical parameters for the core region, for which the values are listed in Table II.

Convective thermal boundary conditions at surfaces of the battery case are applied. Accordingly, boundary conditions for the battery core are,

$$-k_z\frac{\partial T}{\partial z} = \left[\frac{1}{h_{z,0}} + \frac{l_c}{k_c}\right]^{-1}(T - T_0) \quad \text{at} \quad z = 0 \qquad [4a]$$

$$+k_z\frac{\partial T}{\partial z} = \left[\frac{1}{h_{z,L}} + \frac{l_c}{k_c}\right]^{-1}(T - T_0) \quad \text{at} \quad z = L \qquad [4b]$$

$$-k_r\frac{\partial T}{\partial r} = 0 \quad \text{at} \quad r = 0 \qquad [4c]$$

$$+k_r\frac{\partial T}{\partial r} = \left[\frac{1}{h_r} + \frac{l_c}{k_c}\right]^{-1}(T - T_0) \quad \text{at} \quad r = R \qquad [4d]$$

where l_c and k_c denote the thickness and the thermal conductivity of the battery case, respectively. The environment temperature is represented

Table II. Thermophysical properties, entropic heat generation coefficients, and apparent DC resistance for the battery core.[1]

Parameter	k_r [W m^{-1} K^{-1}]	k_z [W m^{-1} K^{-1}]	ρ [kg m^{-3}]	c_p [J kg^{-1} K^{-1}]	$dV_{oc,p}/dT$ [V K^{-1}]	$dV_{oc,n}/dT$ [V K^{-1}]	R_d [mΩ]
Values	0.74	0.85	3900	1882	-1.0×10^{-3}	-6.3×10^{-4}	3

by T_0. The convective heat transfer coefficients at the bottom, top, and lateral surface of the battery are denoted by $h_{z,0}$, $h_{z,L}$, and h_r, respectively.

The initial temperature of the battery is assumed the same as the environment temperature T_0;

$$T = T_0 \quad \text{at} \quad t = 0 \qquad [5]$$

Although a constant ambient temperature is assumed here, the method allows definition of ambient temperature as a function of both space and time.[18]

During charging process of a NiMH battery, two sets of reactions occur in positive and negative electrodes, as listed below;

- Primary reactions:

$$\text{Negative}: \ H_2O + M + e^- \rightarrow OH^- + MH \qquad [6a]$$

$$\text{Positive}: \ Ni(OH)_2 + OH^- \rightarrow NiO(OH) + H_2O + e^- \qquad [6b]$$

- Side reactions:

$$\text{Negative}: \ \frac{1}{2}O_2 + H_2O + 2e^- \rightarrow 2OH^- \qquad [7a]$$

$$\text{Positive}: \ 2OH^- \rightarrow \frac{1}{2}O_2 + H_2O + 2e^- \qquad [7b]$$

The main reactions involve the redox reaction of the metal hydride material at the negative electrode and the redox reaction of the nickel active material at the positive electrode. Oxygen reduction and oxygen evolution are the side reactions that occur in negative and positive electrodes, respectively.[20]

During regular charging, the primary charging reactions are dominant at the electrodes, and the overall reaction is,

$$Ni(OH)_2 + M \rightarrow NiO(OH) + MH - 14.65\,[\text{kJ mol}^{-1}] \qquad [8]$$

while during overcharging, the side reactions become dominant, i.e., the oxygen generated at the positive electrode reacts with hydrogen at the negative electrode to form water [cf. Eq. (9)] and release plenty of combination heat.[21]

$$2H + \frac{1}{2}O_2 \rightarrow H_2O - 285.9\,[\text{kJ mol}^{-1}] \qquad [9]$$

Since heat generation rate in regular charging and overcharging processes are different, we calculate them differently with the following formulas;[1,22]

$$\dot{g} = \begin{cases} \dfrac{I}{\mathscr{V}}\left(V - V_{oc} + T\dfrac{dV_{oc}}{dT}\right) & \text{regular charging} \\ \dfrac{1}{\mathscr{V}}\left(R_d I^2 + nF\Delta H\right) & \text{overcharging} \end{cases} \qquad [10]$$

The parameters I and V denote operational current and voltage of the battery, and $\mathscr{V}$ is the battery volume. Open circuit voltage (OCV) of the battery, also known as equilibrium potential, is denoted by V_{oc}. The constants $R_d = 3$ mΩ (see Table II), $n = 0.5$, $F = 96487$ A s/mol, and $\Delta H = 285.9$ k J/mol denote apparent DC resistance of the battery, electric charge number, the Faraday constant, and enthalpy of the recombination reaction [cf. Eq. (9)], respectively.[1,24]

During regular charging, the heat generation consists of irreversible heat $I(V - V_{oc})/\mathscr{V}$ due to polarization and ohmic potential loss and reversible heat $IT\,(dV_{oc}/dT)\,/\mathscr{V}$ due to the entropy change in electrochemical reactions. Note that, during battery operation $V - V_{oc}$ varies with time, thus the irreversible heat generation term is an explicit function of time and the reversible heat generation term explicitly depends on temperature and implicitly depends on time and spatial variables, i.e., r and z, via temperature. During overcharging period, the heat generation involves Joule heating $R_d\,I^2/\mathscr{V}$, and recombination reaction heat $n\,F\,\Delta H/\mathscr{V}$.

The battery temperature coefficient (entropic heat generation coefficient) dV_{oc}/dT can be presented as,[1]

$$\frac{dV_{oc}}{dT} = \frac{dV_{oc,p}}{dT} - \frac{dV_{oc,n}}{dT} \qquad [11]$$

where the first term on the right hand-side represents the temperature coefficient of the positive electrode and the second term denotes the temperature coefficient of the negative electrode; values are listed in Table II.

Analytical Solution

To simplify the initial-boundary-value problem [cf. Eqs. (3)–(5)] and the corresponding auxiliary equations [cf. Eqs. (10) and (11)], we define a new variable,

$$\theta = T - T_0 \quad \text{thus} \quad d\theta = dT \qquad [12]$$

and rewrite the governing equations in terms of new variable. This gives,

$$\rho c_p \frac{\partial\theta}{\partial t} = k_z\frac{\partial^2\theta}{\partial z^2} + k_r\frac{1}{r}\frac{\partial}{\partial r}\left(r\frac{\partial\theta}{\partial r}\right) + \dot{g} \qquad [13a]$$

with

$$\dot{g} = \begin{cases} \dfrac{I}{\mathscr{V}}\left[V - V_{oc} + (\theta + T_0)\dfrac{dV_{oc}}{d\theta}\right] & \text{regular charging} \\ \dfrac{1}{\mathscr{V}}\left(R_d I^2 + n\,F\,\Delta H\right) & \text{overcharging} \end{cases} \qquad [13b]$$

for which the boundary conditions are,

$$-k_z\frac{\partial\theta}{\partial z} = \left[\frac{1}{h_{z,0}} + \frac{l_c}{k_c}\right]^{-1}\theta \quad \text{at} \quad z = 0 \qquad [14a]$$

$$+k_z\frac{\partial\theta}{\partial z} = \left[\frac{1}{h_{z,L}} + \frac{l_c}{k_c}\right]^{-1}\theta \quad \text{at} \quad z = L \qquad [14b]$$

$$-k_r\frac{\partial\theta}{\partial r} = 0 \quad \text{at} \quad r = 0 \qquad [14c]$$

$$+k_r\frac{\partial\theta}{\partial r} = \left[\frac{1}{h_r} + \frac{l_c}{k_c}\right]^{-1}\theta \quad \text{at} \quad r = R \qquad [14d]$$

and the initial condition is;

$$\theta = 0 \quad \text{at} \quad t = 0 \qquad [15]$$

Equation (13a) that describes the temperature rise θ inside the battery core with respect to the space and time, is solved analytically using the method of integral-transformation, as demonstrated in the successive sessions. The integral-transform technique removes the spatial dependency from the differential equation of heat conduction. In Cartesian coordinate system, this integral-transform is called the Fourier transform, and in the cylindrical coordinate system it is called the Hankel transform.[18]

Fourier Transformation.— The Fourier transform and the inversion formula for the temperature function $\theta(r, z, t)$ with respect to $z \in \{0, L\}$ are defined as;[18]

$$\text{Transformation}: \quad \bar{\theta}(r, \alpha_n, t) = \int_0^L \Phi(\alpha_n, z')\,\theta(r, z', t)\,dz' \qquad [16a]$$

$$\text{Inversion}: \quad \theta(r, z, t) = \sum_{n=1}^{\infty} \Phi(\alpha_n, z)\,\bar{\theta}(r, \alpha_n, t) \qquad [16b]$$

The function $\Phi(\alpha_n, z)$ is the transformation kernel (normalized eigenfunction) in z-direction,

$$\Phi(\alpha_n, z) = \frac{\phi(\alpha_n, z)}{\sqrt{N_z}} \quad [17]$$

and $\phi(\alpha_n, z)$ is the eigenfunction;

$$\phi(\alpha_n, z) = \alpha_n \cos(\alpha_n z) + H_{z,0} \sin(\alpha_n z) \quad [18]$$

The eigenfunction is solution of the following Sturm–Liouville system corresponding to Eqs. (13a), (14a), and (14b)

,

$$\frac{d^2\phi}{dz^2} + \alpha_n^2 \phi = 0 \quad [19a]$$

$$-\frac{d\phi}{dz} + H_{z,0}\phi = 0 \quad \text{at} \quad z = 0 \quad [19b]$$

$$+\frac{d\phi}{dz} + H_{z,L}\phi = 0 \quad \text{at} \quad z = L \quad [19c]$$

where $H_{z,0} = h_{z,0}/k_z$ and $H_{z,L} = h_{z,L}/k_z$. In Eqs. (16)–(19), α_n indicates the n-th eigenvalue in z-direction. The eigenvalues are positive roots (infinite) of the following transcendental equation;[18]

$$\tan(L\alpha_n) = \frac{\alpha_n \left(H_{z,0} + H_{z,L}\right)}{\alpha_n^2 - H_{z,0} H_{z,L}} \quad [20]$$

Eigenvalues normalization factor N_z, which appears in Eq. (17) is obtained as;[18]

$$N_z = \frac{1}{2}\left[\frac{H_{z,0}}{\alpha_n^2} + \frac{\alpha_n^2 + H_{z,0}^2}{\alpha_n^2}\left(L + \frac{H_{z,L}}{\alpha_n^2 + H_{z,L}^2}\right)\right] \quad [21]$$

The integral-transform of the initial-boundary-value problem [cf. Eqs. (13)–(15)], according to transformation (16a), yields the following PDE for $\bar{\theta}$;

$$\rho c_p \frac{\partial \bar{\theta}}{\partial t} = -k_z \alpha_n^2 \bar{\theta} + k_r \frac{1}{r}\frac{\partial}{\partial r}\left(r \frac{\partial \bar{\theta}}{\partial r}\right) + \bar{\bar{g}} \quad [22a]$$

with

$$\bar{\bar{g}} = \begin{cases} \dfrac{I}{\mathscr{V}} \displaystyle\int_0^L \Phi(\alpha_n, z)\left(V - V_{oc} + T_0 \frac{dV_{oc}}{d\theta}\right) dz \\ \quad + \dfrac{I}{\mathscr{V}} \bar{\theta} \dfrac{dV_{oc}}{d\theta} & \text{regular charging} \\ \dfrac{1}{\mathscr{V}} \displaystyle\int_0^L \Phi(\alpha_n, z)\left(R_d I^2 + nF\Delta H\right) dz & \text{overcharging} \end{cases} \quad [22b]$$

The transformed boundary conditions are,

$$-k_r \frac{\partial \bar{\theta}}{\partial r} = 0, \quad \text{at} \quad r = 0 \quad [23a]$$

$$+k_r \frac{\partial \bar{\theta}}{\partial r} = \left[\frac{1}{h_r} + \frac{l_c}{k_c}\right]^{-1} \bar{\theta}, \quad \text{at} \quad r = R \quad [23b]$$

and the transformed initial condition is,

$$\bar{\theta} = 0, \quad \text{at} \quad t = 0 \quad [24]$$

where $\bar{\theta} \equiv \bar{\theta}(r, \alpha_n, t)$, and quantities with a bar refer to transformed quantities as given in Eq. (16a). Due to the Fourier transformation, in Eq. (22) the derivative term with respect to z is transformed to an algebraic term, thus, boundary conditions in z-direction are not required.

Henkel Transformation.— Equations (22)–(24) include differential operator with respect to radial direction $r \in \{0, R\}$ which can be transformed to algebraic terms by means of Henkel transform. The Henkel transform and its corresponding inversion formula are;[18]

$$\text{Transformation}: \quad \bar{\bar{\theta}}(\beta_m, \alpha_n, t) = \int_0^R r' \Psi(\beta_m, r') \bar{\theta}(r', \alpha_n, t)\, dr' \quad [25a]$$

$$\text{Inversion}: \quad \bar{\theta}(r, \alpha_n, t) = \sum_{m=1}^{\infty} \Psi(\beta_m, r)\, \bar{\bar{\theta}}(\beta_m, \alpha_n, t) \quad [25b]$$

Here, the quantities with two bars are transferred by Eq. (16a) and Eq. (25a); first bar denotes the Fourier transform and the second one Henkel transform.

The function $\Psi(\beta_m, z)$ is the transformation kernel (normalized eigenfunction) in r-direction;

$$\Psi(\beta_m, r) = \frac{\psi(\beta_m, r)}{\sqrt{N_r}} \quad [26]$$

and $\psi(\beta_m, r)$ is the eigenfunction,

$$\psi(\beta_m, r) = J_0(\beta_m r) \quad [27]$$

The eigenfunction is solution of the following homogenous eigenvalue problem in r-direction,[18]

$$\frac{d}{dr}\left(r \frac{d\psi}{dr}\right) + \beta_m^2 r \psi = 0 \quad [28a]$$

$$-\frac{d\psi}{dr} = 0 \quad \text{at} \quad r = 0 \quad [28b]$$

$$+\frac{d\psi}{dr} + H_r \psi = 0 \quad \text{at} \quad r = R \quad [28c]$$

in which $H_r = h_r/k_r$. In Eqs. (25)–(28), β_m denotes the m-th eigenvalue in r-direction. The eigenvalues are positive roots of the following transcendental equation,[18]

$$\beta_m \left.\frac{d\, J_0(r)}{dr}\right|_{\beta_m R} = -H_r\, J_0(\beta_m R) \quad [29]$$

in which J_0 is the Bessel function of the first kind.

Eigenvalues normalization factor N_r [cf. Eq. (26)] is evaluated as;

$$N_r = \frac{R^2}{2}\left[1 + \frac{H_r^2}{\beta_m^2}\right] J_0^2(\beta_m R) \quad [30]$$

The integral transform of Eqs. (22)–(24), according to the transformation (25a), yields the following ODE for $\bar{\bar{\theta}}$;

$$\rho c_p \frac{d\bar{\bar{\theta}}}{dt} = -\Delta_{m,n} \bar{\bar{\theta}} + \bar{\bar{\bar{g}}} \quad [31a]$$

with

$$\Delta_{m,n} = \begin{cases} k_z \alpha_n^2 + k_r \beta_m^2 + \dfrac{I}{\mathscr{V}} \dfrac{dV_{oc}}{d\theta} & \text{charging} \\ k_z \alpha_n^2 + k_r \beta_m^2 & \text{overcharging} \end{cases} \quad [31b]$$

and

$$\bar{\bar{\bar{g}}} = \begin{cases} \dfrac{I}{\mathscr{V}} \displaystyle\int_0^R \int_0^L r\, \Psi(\beta_m, r)\, \Phi(\alpha_n, z) \\ \quad \times \left(V - V_{oc} + T_0 \dfrac{dV_{oc}}{d\theta}\right) dz\, dr & \text{regular charging} \\ \dfrac{1}{\mathscr{V}} \displaystyle\int_0^R \int_0^L r\, \Psi(\beta_m, r)\, \Phi(\alpha_n, z) \\ \quad \times \left(R_d I^2 + n\, F\, \Delta H\right) dz\, dr & \text{overcharging} \end{cases} \quad [31c]$$

The required initial condition for the ODE is,

$$\bar{\bar{\theta}} = 0 \quad \text{at} \quad t = 0 \qquad [31d]$$

where $\bar{\bar{\theta}} \equiv \bar{\bar{\theta}}(\beta_m, \alpha_n, t)$.

Inversion of the Transformed Temperature Function.— Using the Fourier and the Henkel transforms, the original PDE of heat conduction [cf. Eq. (3)] is converted to an inhomogeneous first-order ODE [cf. Eq. (31a)] for the double transformed temperature function $\bar{\bar{\theta}}(\beta_m, \alpha_n, t)$, subject to the prescribed initial condition as given by Eq. (31d). An exact solution for Eq. (31a) is straightforward to be obtained, that is,

$$\bar{\bar{\theta}}(\beta_m, \alpha_n, t) = \exp\left(-\frac{\Delta_{m,n}}{\rho c_p} t\right)\left[\int_t \frac{\bar{\bar{g}}(t)}{\rho c_p} \exp\left(\frac{\Delta_{m,n}}{\rho c_p} t\right) dt + \mathscr{C}\right] \qquad [32]$$

for which the corresponding integrating constant $\mathscr{C}$ must be evaluated from the given initial condition, $\bar{\bar{\theta}}(\beta_m, \alpha_n, 0) = 0$.

When the above solution is inverted successively by means of inversion formulas, i.e., Eqs. (16b) and (25b), a series form solution for the original problem can be obtained as;

$$\theta(r, z, t) = \sum_{m=1}^{\infty}\sum_{n=1}^{\infty} \Psi(\beta_m, r)\, \Phi(\alpha_n, z)\, \bar{\bar{\theta}}(\beta_m, \alpha_n, t) \qquad [33]$$

Results and Discussion

In this section, the thermal behavior of the sample NiMH battery during fast-charging process is investigated by the proposed analytical approach. The required calculations, as explained in previous, are programmed symbolically in MATHEMATICA (Version 9.0)[19] to obtain a generic solution for temperature field inside the battery core. Comparing with the existing mutli-dimensional numerical approaches, e.g. Refs. 1–3, 6, and 25, the developed analytical model requires minimum numerical effort, which is needed for evaluation of eigenvalues from transcendental equations [cf. Eqs. (20), (29)]. Solutions for the temperature distribution inside the battery, as given in Eq. (33), are obtained and compared to the experimental data from Ref. 1, and numerical results.

Model Validation with Experimental Data.— The voltage response of the considered NiMH battery during charging processes at 8 A, 18 A, and 32 A is reported in Ref. 1, demonstrates by symbols in Fig. 2. Note that, since the capacity of the battery is 8 Ah, the charging

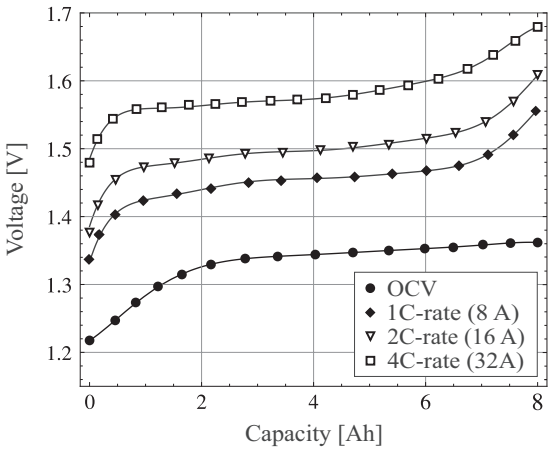

Figure 2. Variations of the battery voltage versus capacity (Ah) are shown during charging processes. Symbols indicate the data borrowed from Ref. 1, for open-circuit voltage (black circles), 8 A charging current (black diamonds), 16 A charging current (white triangles), and 32 A charging current (white squares). Solid lines represent sixth-order polynomial fits to the actual data.

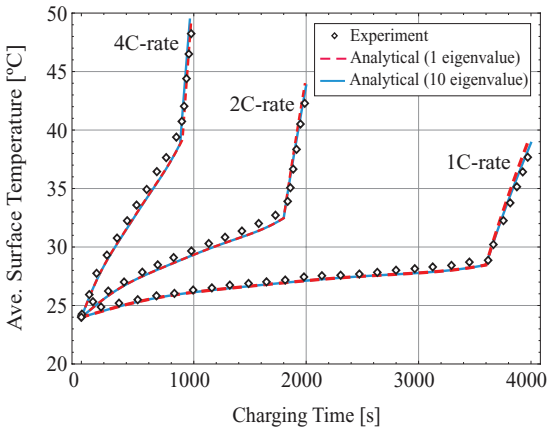

Figure 3. Calculated average surface temperature profiles of the battery core during charge at 1C, 2C, and 4C constant current are compared to experimental temperature measurements (symbols).[1] Analytical temperature distributions are denoted by dashed-line (red) for first term approximation and solid lines (blue) for series solution. A forced-convection cooling is considered at all surfaces of the battery, $h_{z,0} = h_{z,L} = h_r = 25$ W m^{-2} K^{-1}, and the ambient and initial temperature of 24°C is assumed.

time at 8 A, 16 A, and 32 A correspond to 3600, 1800, and 900 seconds, respectively. A sixth-order polynomial is fitted to each constant current charging process as presented with lines in Fig. 2. These polynomials are used to evaluate the irreversible heat generation $I(V - V_{oc})/\mathscr{V}$ term, in Eq. (10).

Figure 3 compares the measured surface average temperature profiles of the battery core during charge at 1C, 2C, and 4C constant current, borrowed from Ref. 1, with the ones obtained from the analytical model, at varying charging times under forced-convection cooling at all battery surfaces, $h_{z,0} = h_{z,L} = h_r = 25$ W m^{-2} K^{-1}. The sharp increase in the temperature corresponds to the overcharging period when the recombination reaction heat is involved [cf. Eq. (10)]. From the temperature trend, one can conclude that the total heat generation rate increases slowly during charging period and jumps quickly thereafter. When the cell is under charging, the reversible and irreversible heats (due to primary reactions) contribute to the total heat generation rate. When the cell is under overcharging, the heat generation rate increases dramatically because the enthalpy potentials of recombination reaction is comparably large [cf. Eqs. (8), (9)]. Initially, the recombination reaction is negligible, and all the current applied to the cell is used to convert the active materials from discharge to charge state. When charge input exceeds 100% of nominal cell capacity, the rate of primary reaction current decreases, while the total current remaining the same, consequently, the recombination reaction and the corresponding heat generation rate become significant. Relative effects of heat generation terms in NiMH batteries are thoroughly discussed in Ref. 23, using a detailed thermo-electrochemical model.

Figure 3 shows an excellent agreement between the analytical results and experimental measurements. The comparison shows that even the first-term approximation (one eigenvalue) is accurate enough to predict the average surface temperature of the battery and further increase in the number of eigenvalues will not have any significant impact on the results accuracy.

The inconsistency between the measured and calculated temperature values at the later times of the overcharging processes, is related to the fact that the rate of heat generation during overcharging period is overestimated in Eq. (10); because only part of generated oxygen at the positive electrode is reduced at the negative electrode.[1] Moreover, in the proposed analytical model, the battery thermal capacity, c_p, is assumed to be independent of temperature, and the thermal conductivity of the porous materials is approximated by averaging, as given in Eq. (1) however in reality, due to the pores distribution and their size, the thermal conductivities may vary in different locations.

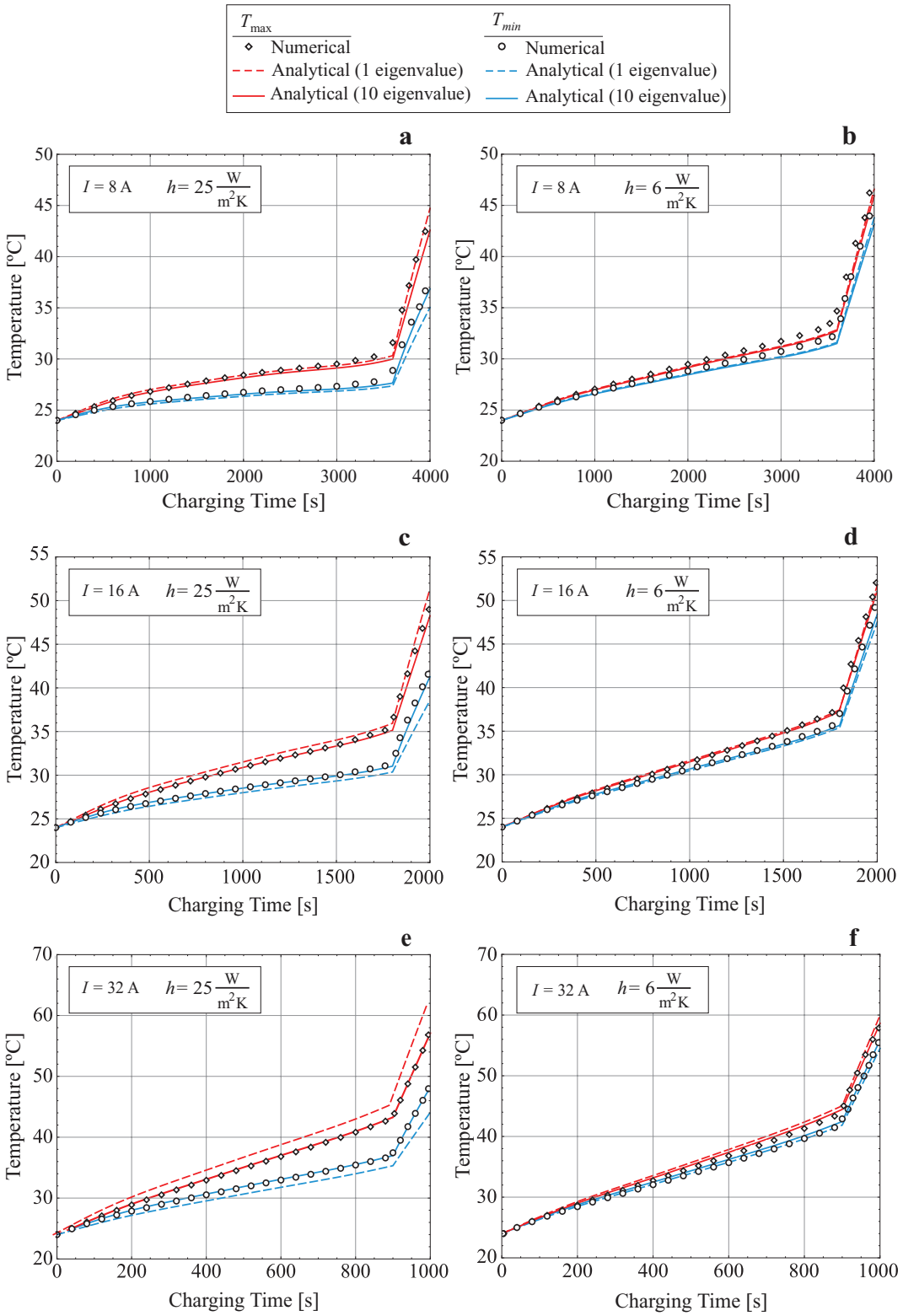

Figure 4. Temperature variation vs. time is shown for different charge rates. Maximum temperature at the battery center (red lines) and minimum temperature at the battery rim (blue lines) are compared to numerical data for maximum and minimum temperature (symbols). In plots (a)-(f), thermal response of the battery during 8 A, 16 A, and 32 A charge current is shown for small and moderate heat transfer coefficients considered at all surfaces $h_{z,0} = h_{z,L} = h_r = \{6, 25\}$ W m^{-2} K^{-1}. The dashed lines represent the analytical results with first term approximation and solid lines indicate the series solution results.

Model Validation with Numerical Data.— Variation of maximum temperature T_{max} at the center of the battery and minimum temperature T_{min} at the rim of the battery as a function charging time are shown in fig. 4. A convective heat transfer with small and moderate heat transfer coefficients is assumed at all surfaces of the battery case, $h_{z,0} = h_{z,L} = h_r = \{6, 25\}$ W m^{-2} K^{-1}; and both ambient and initial conditions are set to $T_0 = 24$°C. The temperatures T_{max} and T_{min} calculated numerically with a finite element PDE solver (COMSOL MULTIPHYSICS, Version 4.3b), shown with symbols, are used to validate the results obtained from the proposed analytical model,

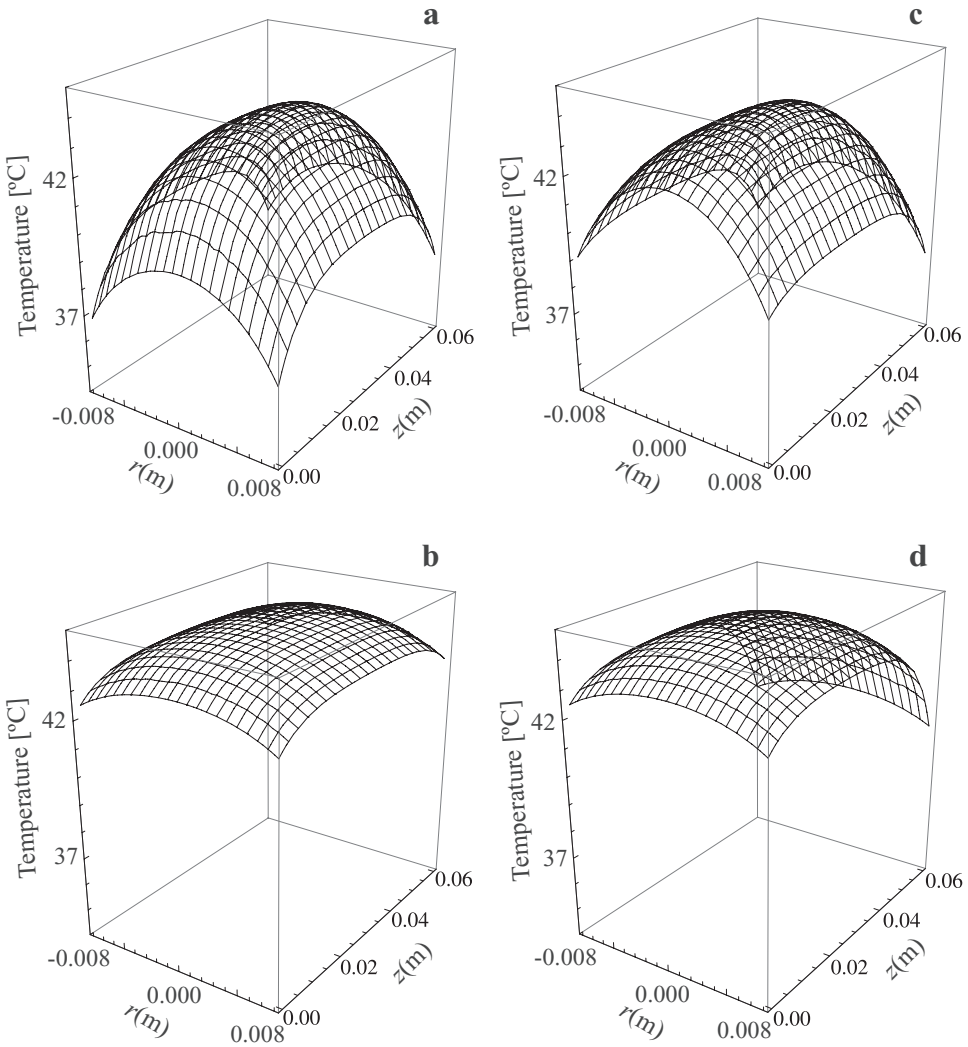

Figure 5. Two-dimensional temperature profile at the end of 32 A charge process is plotted for a) forced-convection at all surfaces $h_{z,0} = h_{z,L} = h_r = 25$ W m^{-2} K^{-1}, b) natural-convection at all surfaces $h_{z,0} = h_{z,L} = h_r = 6$ W m^{-2} K^{-1}, c) forced-convection at top and lateral surfaces $h_{z,L} = h_r = 25$ W m^{-2} K^{-1} and natural-convection at the bottom surface $h_{z,0} = 6$ W m^{-2} K^{-1}, and d) forced-convection at the top surface $h_{z,L} = 25$ W m^{-2} K^{-1} and natural-convection at other surfaces $h_{z,0} = h_r = 6$ W m^{-2} K^{-1}. Ambient and initial temperature of 24$^{\circ}C$ is assumed.

shown with lines. Both analytical and numerical computations were performed on a single processor PC, with a 64-bit quad-core CPU (Core i7) and 10GB of RAM.

Since thermal conduction inside the battery is a diffusion process and sharp temperature gradients do not form inside the computational domain, the numerical solution is not very sensitive to the resolution of computational grid. The difference between calculated temperatures with a course grid (82 elements) and a fine grid (6680 elements) was about 0.001 °C, while the relative tolerance was set to 10^{-10}. For the case of 1C-rate charging (a 60-minute process) the numerical simulation time varied from a few seconds with the coarse grid to about two minutes with the fine grid.

For our analytical solutions we used built-in functions in MATHEMATICA to calculate the eigenvalues and to integrate the functions. Computations with a single eigenvalue in each direction take fraction of a second; nonetheless, with increase in the number of eigenvalues the computing effort becomes comparable to numerical model. It is important to mention that unlike numerical simulations, the computational time in analytical simulations is independent of the actual process time.

The battery thermal responses at 8 A charging are plotted in figs. 4a and b, whereas figs. 4c and d represent the same information for 16 A charging current, and figs. 4e and f correspond to the same data at 32 A charging current. Two sets of the analytical results are presented for T_{max} and T_{min}, in which the dashed lines denote the analytical solution with the first eigenvalue in each direction only, i.e., the first term approximation, and the solid lines show the analytical solution with 10 eigenvalues, i.e., series solution. The comparisons show a fair agreement between the analytical and numerical results. From fig. 4, one can conclude that the proposed analytical model is able to provide an acceptable accuracy with minimum computational effort which takes only a fraction of seconds. In other word, the main advantage of the developed analytical model, is that only the first eigenvalue in each direction is sufficient to predict the thermal behavior of the battery under different conditions in terms of charging current and convective cooling (natural or forced-convection).

Effect of Convective Cooling on Temperature Distribution.— In Fig. 5, two-dimensional temperature profile at the end of charging at 32 A is shown. Plot (a) presents the temperature distribution when a forced convection is applied at all surfaces of the battery case, $h_{z,0} = h_{z,L} = h_r = 25$ W m^{-2} K^{-1}, while plot (b) present the temperature distribution when all the surfaces are faced to a natural-convection, $h_{z,0} = h_{z,L} = h_r = 6$ W m^{-2} K^{-1}. Plot (c) belongs to the case in which a forced-convection is assumed on top and lateral boundaries, $h_{z,L} = h_r = 25$ W m^{-2} K^{-1}, and a natural-convection

on bottom boundary, $h_{z,0} = 6$ W m^{-2} K^{-1}, whereas plot (d) corresponds to the case in which a forced-convection is only used at the top boundary, $h_{z,L} = 25$ W m^{-2} K^{-1}, and natural-convection on the other boundaries, $h_{z,0} = h_r = 6$ W m^{-2} K^{-1}. The latter cases are defined to examine the effects of non-uniform boundary conditions on the temperature distribution. By comparing plots (a) with (b), we can conclude that although the battery temperature is markedly lower under forced-convection than natural-convection, when the charging process is under natural-convection the temperature gradient is not as pronounced as that under forced-convection, note the difference between minimum and maximum values of temperature. However, a more uniformed temperature distribution and a high heat dissipation rate are predicted in plot (c) when forced-convection is applied at the top and lateral surfaces of the battery case. Furthermore, Plot (d) shows that applying forced-convection only at the top boundary cannot be sufficient to dissipate the generated heat.

Conclusions

Applying integral-transform technique, a closed-form analytical model is proposed to investigate the temperature distribution in spirally wound batteries with modest numerical effort. The developed thermal model takes account for:

- multi-dimensional heat conduction,
- orthotropic thermal conductivities,
- time dependent and temperature dependent heat generation terms,
- convective boundary conditions,

thus, it provides a robust tool for studying the thermal behavior of the batteries in various operating conditions.

The developed model was employed to study the temperature rise in a 8 Ah cylindrical NiMH cell during fast-charging processes with an overcharging periods at 1C (8 A), 2C (16 A), and 4C (32 A)-rates, where the transient heat generation during charging period was approximated from the electrical performance of the battery.

The accuracy of the model was validated by comparing with experimental and numerical data. The comparisons confirmed that even the first term of the series solution suffices to accurately describe the two-dimensional temperature distribution inside the battery core with the modest computational effort. Hence, the proposed model can be considered as a robust tool for studying the thermal behavior of the spirally wound batteries in various operating conditions.

From the overcharge modeling, a sharp rise in the battery temperature was reported which is as a result of recombination heat; therefore, in fast-charging NiMH batteries, it is recommended to avoid overcharging. Furthermore, the results obtained from the proposed model demonstrated that, the heat dissipation can be improved by applying a forced-convection cooling at all battery surfaces, however it can increase the temperature gradient. The modeling of non-uniform boundary conditions suggested that a natural-convection at the bottom surface and forced-convection at the other surfaces of the battery, can result in a more uniform temperature and a high rate of heat dissipation.

To conclude, it is essential to point out that the major limitation of the developed thermal model is the necessity of linear boundary conditions. This limit that is defined by Sturm–Liouville theory, implies that heat transfer coefficient h must be constant on the surface. In reality, when the batteries are horizontally arranged in the battery pack, the convective heat transfer coefficient h varies over battery surfaces, because the cooling fluid follows the curvature of the battery and this complicated flow pattern influences heat transfer coefficient. Thus, the heat transfer coefficient will vary along the circumference of the battery (in φ-direction).

Acknowledgment

This work was financially supported by Automotive Partnership Canada (APC), grant No. APCPJ 401826-10.

List of Symbols

c_p	heat capacity (J kg^{-1}K^{-1})
F	Faraday constant (A s mol^{-1})
$\dot{g}$	heat generation rate (W m^{-3})
H	ratio of convective to conduction heat transfer coefficients, h/k (m^{-1})
ΔH	standard enthalpy of formation (kJ mol^{-1})
h	convective heat transfer coefficients at surfaces (W m^{-2} K^{-1})
I	total charge/discharge current (A)
k	thermal conductivity (W m^{-1} K^{-1})
L	height of battery core (m)
l_c	thickness of can (mm)
N	normalization factor for eigenfunction
n	electric charge number
R	radius of battery core (m)
R_d	internal resistance (Ω)
r	position in r-direction (m)
T	core temperature (°C)
T_0	ambient and initial temperatures (°C)
t	time (s)
V	operational battery voltage (V)
V_{oc}	open circuit potential (V)
$\mathscr{V}$	volume of the battery core (m^3)
z	position in z-direction (m)
NiMH	nickel-metal hydride
OCV	open circuit voltage

Greek

α	eigenvalues in z-direction
β	eigenvalues in r-direction
ε	porosity
θ	temperature difference (°C)
ν	volume fraction
ρ	mass density (kg m^{-1})
Φ	transformation kernel in z-direction
ϕ	eigenfunction in z-direction
Ψ	transformation kernel in r-direction
ψ	eigenfunction in r-direction
φ	azimuthal direction

Superscript

c	related to battery case
f	related to liquid filler (electrolyte)
m	related to structural materials
n	related to negative electrode
p	related to positive electrode
s	related to separator
$\bar{}$	transformed quantity based on Eq. (16a)
$\tilde{}$	transferred quantity based on Eq. (25a)

References

1. J. Shi, F. Wu, S. Chen, and C. Zhang, *J. Power Sources*, **157**, 592 (2006).
2. Y. Inui, Y. Kobayashi, Y. Watanabe, Y. Watase, and Y. Kitamura, *Energy Convers. Manage.*, **48**, 2103 (2007).
3. D. H. Jeon and S. M. Baek, *Energy Convers. Manage.*, **52**, 2973 (2011).
4. K.-J. Lee, K. Smith, A. Pesaran, and G.-H. Kim, *J. Power Sources*, **241**, 20 (2013).
5. S. A. Hallaj, H. Maleki, J. Hong, and J. Selman, *J. Power Sources*, **83**, 1 (1999).
6. D. Li, K. Yang, S. Chen, and F. Wu, *J. Power Sources*, **184**, 622 (2008).

7. P. M. Gomadam, R. E. White, and J. W. Weidner, *J. Electrochem. Soc.*, **150**, A1339 (2003).
8. T. I. Evans and R. E. White, *J. Electrochem. Soc.*, **136**, 2145 (1989).
9. E. E. Kalu and R. E. White, *J. Electrochem. Soc.*, **140**, 23 (1993).
10. T. D. Hatchard, D. D. MacNeil, A. Basu, and J. R. Dahn, *J. Electrochem. Soc.*, **148**, A755 (2001).
11. R. Mahamud and C. Park, *APPL MATH MODEL*, **37**, 2787 (2013).
12. P. Taheri, M. Yazdanpour, and M. Bahrami, *J. Power Sources*, **245**, 712 (2014).
13. P. Taheri, M. Yazdanpour, and M. Bahrami, *J. Power Sources*, **243**, 280 (2013).
14. K. Fang, D. Mu, S. Chen, F. Wu, and X. Zeng, *J. Therm. Anal. Calorim.*, **105**, 383 (2011).
15. M. Wu, Y. Wang, and C. Wan, *J. Power Sources*, **74**, 202 (1998).
16. P. M. Gomadam, J. W. Weidner, R. A. Dougal, and R. E. White, *J. Power Sources*, **110**, 267 (2002).
17. J. Kim, T. V. Nguyen, and R. E. White, *J. Electrochem. Soc.*, **139**, 2780 (1992).
18. M. N. Özisik, *Boundary value problems of heat conduction*, Dover Publications, New York, 1989.
19. Mathematica Research, Inc., Mathematica, Version 9.0, Champaign, IL (2012).
20. B. Wu, M. Mohammed, D. Brigham, R. Elder, and R. White, *J. Power Sources*, **101**, 149 (2001).
21. K. Fang, D. Mu, S. Chen, B. Wu, and F. Wu, *J. Power Sources*, **208**, 378 (2012).
22. D. Bernardi, E. Pawlikowski, and J. Newman, *J. Electrochem. Soc.*, **132**, 5 (1985).
23. W. B. Gu and C. Y. Wang, *J. Electrochem. Soc.*, **147**, 2910 (2000).
24. N. Sato and K. Yagi, *JSAE Review*, **21**, 205 (2000).
25. Q. Wang, P. Ping, X. Zhao, G. Chu, J. Sun, and C. Chen, *J. Power Sources*, **208**, 210 (2012).